Modeling of intracerebral interictal epileptic discharges

Clinical Neurophysiology 129 (2018) 1276–1290

Contents lists available at ScienceDirect

Clinical Neurophysiology

journal homepage: www.elsevier.com/locate/clinph

Modeling of intracerebral interictal epileptic discharges: Evidence for network interactions

Stephan Meesters [a,b,*], Pauly Ossenblok [a,c], Albert Colon [a], Louis Wagner [a], Olaf Schijns [a,d], Paul Boon [a], Luc Florack [b], Andrea Fuster [b]

[a] Academic Center for Epileptology Kempenhaeghe & Maastricht University Medical Center, The Netherlands
[b] Department of Mathematics & Computer Science, Eindhoven University of Technology, The Netherlands
[c] Department of Biomedical Engineering, Eindhoven University of Technology, The Netherlands
[d] Department of Neurosurgery, Maastricht University Medical Center, The Netherlands

ARTICLE INFO

Article history:
Accepted 16 March 2018
Available online 11 April 2018

Keywords:
Stereo-electroencephalography
Analysis framework
Interictal epileptic discharges
Spatiotemporal network interaction
Epilepsy surgery

HIGHLIGHTS

- A framework is introduced to model network interactions underlying interictal epileptic discharges.
- Interdependency of brain areas is assessed by independent component analysis of synchronized spikes.
- It is concluded that a network approach is promising in the case of complex epilepsies.

ABSTRACT

Objective: The interictal epileptic discharges (IEDs) occurring in stereotactic EEG (SEEG) recordings are in general abundant compared to ictal discharges, but difficult to interpret due to complex underlying network interactions. A framework is developed to model these network interactions.
Methods: To identify the synchronized neuronal activity underlying the IEDs, the variation in correlation over time of the SEEG signals is related to the occurrence of IEDs using the general linear model. The interdependency is assessed of the brain areas that reflect highly synchronized neural activity by applying independent component analysis, followed by cluster analysis of the spatial distributions of the independent components. The spatiotemporal interactions of the spike clusters reveal the leading or lagging of brain areas.
Results: The analysis framework was evaluated for five successfully operated patients, showing that the spike cluster that was related to the MRI-visible brain lesions coincided with the seizure onset zone. The additional value of the framework was demonstrated for two more patients, who were MRI-negative and for whom surgery was not successful.
Conclusions: A network approach is promising in case of complex epilepsies.
Significance: Analysis of IEDs is considered a valuable addition to routine review of SEEG recordings, with the potential to increase the success rate of epilepsy surgery.

1. Introduction

About 30% of the epilepsy patients are drug-resistant (Mohanraj and Brodie, 2006), of which half are potential candidates for epilepsy surgery. If non-invasive examinations, such as video-EEG seizure monitoring and MRI, do not result in a single hypothesis on the epileptogenic zone then the patient may become a candidate for preoperative invasive EEG recordings. Furthermore, if there are multiple hypotheses on possible locations of the epileptogenic zone or if the epilepsy is suspected to originate in deep-sited anatomical structures, depth electrode or stereotactic EEG (SEEG) recordings (Talairach et al., 1992) are considered to be the best choice.

The clinical assessment of SEEG recordings is primarily aimed at identifying the brain area that is responsible for the seizures of the patient, the so-called seizure onset zone (SOZ). Knowledge of the

Abbreviations: SEEG, stereo-electroencephalography; IED, interictal epileptic discharges; GLM, General Linear Model; ICA, Independent Component Analysis; SOZ, seizure onset zone.

* Corresponding author at: MetaForum 7.077, P.O. Box 513, 5600 MB Eindhoven, The Netherlands. Fax: +31 40 247 2753.
E-mail address: s.p.l.meesters@tue.nl (S. Meesters).

https://doi.org/10.1016/j.clinph.2018.03.021
1388-2457/

location of the SOZ and its relation to functional areas, as well as seizure propagation pathways, is crucial for the surgical treatment of drug-resistant epilepsy patients (Bartolomei et al., 2008). To record sufficient seizure activity, long term video-SEEG recording is performed, which is labor-intensive and time-consuming. It may take weeks (typically two to three weeks) to record before conclusions can be drawn regarding the exact location of the SOZ.

There is a vast amount of literature, especially from the Institut de Neurosciences des Systmes Marseille, addressing advanced signal analysis procedures to identify the SOZ based on ictal activity. Bartolomei et al. (2008) reported on the Epileptogenicity Index (EI), which quantifies the appearance of fast oscillations before the seizure starts, and estimated the delay of its appearance with respect to the seizure onset. Following this frequency-based method, it was shown that brain structures that generate a rapid discharge with early involvement during seizures produce a high EI value. However, a later study (Bartolomei et al., 2011) indicated that the EI calculated for different brain areas of patients with temporal lobe seizures disclosed relatively high epileptogenicity in distant cortices, thus indicating a more complex organization of the epileptogenic networks. In a recent review Bartolomei et al. (2017) outlined the concept of the epileptogenic network and the contribution of SEEG signal analysis to this concept, which is mainly based on the analysis of the spatiotemporal dynamics of multiple brain areas involved in the epileptogenic process. Wendling, Bartolomei and coworkers (Wendling et al., 2001a; Bartolomei et al., 2001; Wendling and Bartolomei, 2001) used non-linear correlation methods to characterize the dynamic interactions between neural populations involved in the epileptogenic network, including time delays and directionality of these couplings. The correlation coefficient h^2, introduced by Pijn and Lopes da Silva (1993), da Silva (1989) and further elaborated on by Kalitzin et al. (2007), estimates the non-linear relationship between signals. Similarly to Wendling, Bartolomei and coworkers (Wendling et al., 2001a; Bartolomei et al., 2001; Wendling and Bartolomei, 2001) in the current study the correlation coefficient h^2 is used to estimate the coupling strength. However, a shortcoming of the estimation of time delays based on a time-varying correlation function is that its results may exhibit large variations that are physiologically implausible (van Houdt et al., 2012). Therefore, to overcome this problem, in the current study a regularization procedure is introduced to avoid large variations in the time delay estimated between spatially neighboring signals.

The non-linear correlation studies of couplings between neural populations were mainly introduced for the analysis of seizure activity. However, SEEG recordings also reflect a vast amount of interictal epileptic discharges (IEDs) (Smith, 2005), which are in general abundant compared to ictal discharges. Several methods to analyze interictal activity in SEEG recordings have been reported. The first attempts involved basic techniques such as spectral analysis and linear cross correlation (Alarcon et al., 1994). Later studies (Bourien et al., 2005; Wendling et al., 2009) investigated which brain structures frequently co-activated during the evolvement of IEDs. Amini et al. (2011) used the linear wavelet cross-correlation coefficient as a coupling measure and estimated leading brain areas based on time delays. More recently, Bartolomei et al. (2016) identified the irritative zone (the region which initiates the IEDs) by calculating the spike frequency index (SI) for each brain area involved in the IEDs occurring in SEEG recordings. The SI demonstrated a 75% concordance of the irritative zone and the SOZ in case of cortical dysplasia and 56% concordance in all other cases studied (N = 32). The conclusion of the authors was that when the IEDs arise from complex network interactions the spike frequency index probably is not a suitable descriptor to identify the SOZ.

In the current study a network analysis approach is followed to identify the spatiotemporal interactions of the neuronal populations involved in the IEDs. The time-varying correlation estimated by the non-linear correlation coefficient h^2 is used together with the IED density function as input in the general linear model (GLM) (van Houdt et al., 2012). The output of the GLM indicates the brain areas with SEEG signals that are highly synchronized compared to background activity during the evolvement of the IEDs. To investigate the interdependency of these areas, independent component analysis (ICA) is applied followed by a clustering of its resulting spatial distributions. The averaged spike clusters yield information about the spatiotemporal interactions and the directionality of the interactions, indicating which of the brain areas involved might be related to the SOZ.

The framework of analysis developed in this study was evaluated for five patients who underwent successful surgery. The result of the quantitative analysis of the IEDs of these patients was compared to the SOZ as identified by visual review and the resection that rendered the patient seizure free. Additionally, the analysis was performed for two so-called 'failures', patients for whom the hypothesis based on SEEG recordings did not lead to a satisfactory surgical outcome. The analysis approach as introduced in this study appears to be, especially, suitable to unravel the complex network interactions underlying the IEDs of these patients. Overall, it will be shown that our approach offers the perspective of analyzing interictal SEEG recordings for presurgical evaluation, with the potential to increase the success rate of surgical intervention.

2. Materials and methods

2.1. Patients and electroclinical details

The analysis framework was applied on SEEG recordings of seven patients (N = 7) with drug-resistant epilepsy (see for patient characteristics Table 1). Extensive pre-surgical assessment was performed at the Academic Center for Epileptology, location Kempenhaeghe (Heeze, The Netherlands), including long-term video-EEG monitoring and an epilepsy protocol for 3T MRI measurements to study the presence of anatomical abnormalities (Table 1, column 3). The electro-clinical hypotheses (Table 1, column 4) guided the placement of the depth electrodes. The resection strategy was determined according to the hypothesis of the SOZ (Table 1, column 5), which was based on the standard review of the SEEG recordings. Five of the seven patients included in this study were seizure-free after surgery or had a satisfactory seizure reduction (Engel class 1&2). The follow-up period for seizure assessment was one year. For these five patients there were abnormalities visible at MRI. Further details of these patients can be found in van Houdt et al. (2012), who compared the results of EEG-correlated fMRI analysis to the SEEG recordings of these five patients. The other two patients were diagnosed with an MRI-negative epilepsy and were not seizure free after operation (Engel 3&4). The patient data were acquired solely according to clinical procedures. Each of the patients signed a statement authorizing the anonymous use of his or her clinical data for scientific research.

2.2. Data acquisition and preprocessing

Each patient was implanted with several platinum depth electrodes (DIXI medical, Besanon, France). These electrodes have 5–18 contacts of 2 mm each with an intercontact distance of 1.5 mm. The diameter of the electrodes is 0.8 mm. Besides depth electrodes, in patients 3 and 4 subdural strip electrodes with 4–8

Table 1
Patient characteristics and the clinical hypotheses based on preimplantation neuroradiological (MRI) and electro-clinical examinations of the patients. The resection was guided by the hypothesis regarding the seizure onset zone (SOZ) as result of the presurgical video-SEEG recordings. The outcome of surgery is given for each of the seven patients studied in terms of the Engel Epilepsy Surgery Outcome Scale.

Patients	Age/gender	Lesion	(Electro)-clinical hypothesis	SOZ	Resection	Engel class outcome
1	42/F	Porencephalic cyst frontal R; hippocampal sclerosis R	Temporal R; Parietal R; Insula R	Mesial Temporal R	Anterior temporal R and amygdalohippocampectomy R	2
2	24/M	Hippocampal sclerosis L; infarct occipital L	Temporal L; Occipital L	Mesial Temporal L	Anterior temporal L and amygdalohippocampectomy L	1
3	39/M	Nodular heterotopia occipital L and R; cortical dysplasia mesial temporal R and occipital R	Temporal R; Occipital R	Mesial Temporal R	Anterior temporal R and amygdalohippocampectomy R	2
4	46/F	Hippocampal sclerosis L	Temporal L; Temporoparietal junction L; Insula L	Mesial Temporal L; Lateral Temporal L	Extended anterior temporal L and amygdalohippocampectomy L	1
5	48/M	Infarct Temporo-occipital R	Occipital R; Temporal R	Mesial Temporo-occipital R	Temporo-occipital R	1
6	44/F	Negative	Temporal L; Insula L; Cingulum L	Cingulum L	Anterior Cingulum L	4
7	15/F	Negative	Frontal R; Frontal L	Middle Frontal gyrus (F2) R	Middle Frontal gyrus (F2) R	3

contacts (DIXI medical, Besanon, France) were implanted. A contact in white matter tissue was chosen as the common reference electrode for all channels. The implantation of the electrodes was performed at the Academic Center of Epileptology, location Maastricht University Medical Center (Maastricht, The Netherlands). A pre-implantation structural MRI scan (Intera 3.0 Tesla, Philips Medical Systems, Best, The Netherlands) was acquired with gadolinium contrast-enhancement. After implantation a CT (Sensation 16, Siemens, Berlin, Germany) and structural MR scan (Intera 3.0 Tesla, v.s.) were acquired to verify the positions of the electrodes and the absence of postoperative hematomas. When no further complications occurred, the long-term recording was performed at the Academic Center for Epileptology, location Kempenhaeghe (Heeze, The Netherlands).

The EEG was examined by an experienced EEG specialist who identified on average 471 ± 282 IED's, which amounts to 19.6 ± 11.8 IEDs per hour in the 24 h recordings used. The number of IEDs identified at the SEEG recordings of each of the patients studied is listed in Table 2 (column 2). Isolated IEDs (spikes, sharp waves and spike-and-wave discharges) were annotated at the maximum of the spike amplitude of the IEDs. An interval centered around the maximum of the IEDs was selected with a time duration of 2.5 s. Data was recorded at a sample rate of 600 Hz (Stellate Harmony 6.1 C, Natus Medical Inc., San Carlos, USA). Fieldtrip (Oostenveld et al., 2011) was used to read the data in EDF+ format and to apply bandpass filtering in the frequency range of 1–70 Hz in order to reduce high-frequency noise. Both monopolar and bipolar derivations were created within MATLAB (The MathWorks Inc., Natick, MA, 2015). The SEEG analysis framework developed in this study uses C++, MATLAB and Mathematica 10.0 (Wolfram Research, Inc., Champaign, IL). OpenMP was used for multi-thread processing.

2.3. Overview of the analysis framework

The SEEG analysis, outlined in Fig. 1 (top row), consists of three steps addressing the following questions: (1) is the activity underlying the SEEG signals synchronized during the IEDs? (Section 2.4), (2) which brain areas are involved in the generation of the activity underlying the IEDs? (Section 2.5), and (3) what is the interdependency between multiple active brain areas and can we identify the area that corresponds to the irritative zone? (Section 2.6). Visualization of the analysis results relative to the cortical anatomy is outlined in Fig. 1, bottom row. The methodology is illustrated by the analysis of the SEEG recordings of one of the patients studied.

2.4. Synchronous epileptic activity

To estimate the synchronization of each possible combination of SEEG signals during the occurrence of the IEDs, a non-linear correlation analysis is applied. The correlation coefficient h^2_{XY} is used

Table 2
Results for the patient group, showing the number of IEDs analyzed (#IEDs), the IED activity as determined by visual review and as result of applying the analysis framework (IEDs quantified), and the SOZ as determined as result of visual review of the SEEG recordings. The overlap of IED activity (quantified) with the SOZ is indicated in percentages in the last column. For patients 1 and 7 the overlap is indicated for two focal areas identified. The location is described by the depth electrode label and involved contact points. The depth electrodes are labeled by their anatomical position (e.g. LH = left hippocampus, RH = right hippocampus, RO = right occipital, RP = right parietal, RT = right temporal), which may, in some cases, refer to a different region depending on the patient studied.

Patients	#IEDs	IED activity (visual review)	IED activity (quantified)	SOZ activity	Overlap IED activity (quantified) and SOZ
1	831	RH 2–11; RP 1–3; RF 2–4	Focal areas: (1) RH 3–9; (2) RO 1–6; RP 1–4	RH 7–10	Focal areas: (1) 75%; (2) 0%
2	260	LH 1–6; LH 10–11	LH 1–5	LH 1–11	45%
3	177	RSP 1–3; RH 1–8	RH 1,2,5–8; RSA 1–3; RSL 3–4; RSP 2	RH 6–11	50%
4	883	LH 1–9; LST 2–4; LSO 4–6; LE 6–8	LH 4–8; LE 5–7; LSO 1–5; LST 2–3	LH 7–8; LSP 8	67%
5	502	LH 1–10; RH 1–10; RO 2–6; RZ 1–4; RI 4–6	RO 2–8; RZ 1–7; RI 2–4; RT 3–4	RO 1–6; RZ 1–4	90%
6	270	LH 1–10; LT 3–4; LF 1–2; LP 1–2	LH 6–9; LX 3–9;	LC 2–4	0%
7	379	RY 7–12; RX 8–12; RC 3–8; LC 6–8; LX 9–12	Focal areas: (1) LC 4–8; LX 5–12; LA 14–16; (2) RY 7–12; RX 10–14; RC 4–5,8; RA 6–7,10	RY 10–13; RX 8–12	Focal areas: (1) 56%; (2) 0%

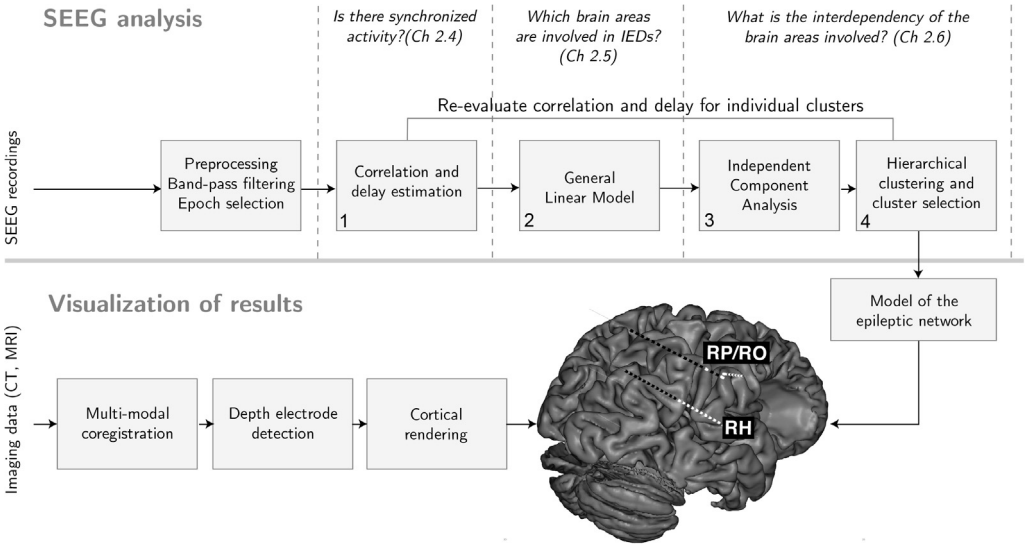

Fig. 1. Overview of the developed methodology, outlining the analysis of SEEG recordings (top) and the visualization of its results (bottom).

in the analysis, which models the degree to which any arbitrary signal Y can be interpreted as a transformed version of signal X (Pijn and Lopes da Silva, 1993; da Silva, 1989; Kalitzin et al., 2007). In other words, we estimate a signal $\widehat{Y}$ given by $\widehat{Y} = S(X)$ where S is the perturbation function. The difference between the true Y and the estimated $\widehat{Y}$ is defined as the unexplained variance. The non-linear coefficient $0 \leqslant h^2_{XY} \leqslant 1$ is then given by

$$h^2_{XY} = \frac{\sum_{i=1}^{n}(Y_i - \overline{Y})^2 - \sum_{i=1}^{n}(Y_i - S(X_i))^2}{\sum_{i=1}^{n}(Y_i - \overline{Y})^2}, \tag{1}$$

where X_i and Y_i are samples of the signals X and Y, respectively, n is the number of samples and $\overline{Y}$ is the average amplitude of signal Y. Originally, the perturbation function S was defined by a piece-wise linear approximation of the regression curve modeled from the scattergram of X and Y (da Silva, 1989). A linear approximation was chosen by these authors because of its computational efficiency. The downside of this method is that the scattergram is required to be divided into bins, which makes its results dependent on the size of the bins. In this study, however, we opt to use a cubic spline instead of a piece-wise linear function, because the cubic spline describes the data better with a lower unexplained variance as result and does not require binning. The parameters of the cubic spline function can be found by using a linear least-squares fit.

The analysis to identify synchronized activity is outlined in a flowchart shown in Fig. 2, top row. The correlation analysis is performed on windows centered around the maximum of the IED (see Fig. 2, top left) with a window size of 250 ms, which is large enough to encompass the IED spike and wave discharges (de Curtis et al., 2012). In addition to the improved perturbation function, in our approach a method is introduced for the accurate estimation of the time delay between the SEEG signals. The time delay is estimated based on the averaged correlation function of all IEDs, as shown in Fig. 2 (top middle), instead of the commonly used time delay estimation based on a single IED (Wendling et al., 2001a). The correlation function is calculated for the time windows of analysis w_k centered around the kth IED, while shifting one signal relative to the other with a time-shift of $-50\text{ ms} \leqslant \tau \leqslant 50\text{ ms}$. The correlation function is denoted by $h^2_{ij}(w_k, \tau_{ij})$, where $(i,j) = 1, \ldots, \#_{\text{contacts}}$ are indices for the depth electrode signals.

The averaged correlation for all IED-centered windows of analysis $\bar{h}^2_{ij}(\tau_{ij})$ is computed according to

$$\bar{h}^2_{ij}(\tau_{ij}) = \frac{1}{N}\sum_{k=0}^{N} h^2_{ij}(w_k, \tau_{ij}), \tag{2}$$

where N is the number of IEDs. From its corresponding graph (see Fig. 2, top middle) the time delay $(\tau_{ij})_{\max}$ is estimated as the time-shift that results in a maximum averaged correlation value:

$$(\tau_{ij})_{\max} = \arg\max_{\tau_{ij}} \ \bar{h}^2_{ij}(\tau_{ij}). \tag{3}$$

Regularization of the delay matrix

However, because multiple local maxima may be present that are nearly equal to the global maximum $\max_{\tau_{ij}} \bar{h}^2_{ij}(\tau_{ij})$ the time delay estimation may be unstable and lead to outliers in the delay matrix. In order to provide a robust estimation of the time delays, a regularization procedure is introduced that incorporates spatial information. In this procedure the average correlation function $\bar{h}^2_{ij}(\tau_{ij})$ is maximized, while simultaneously requiring a certain smoothness between neighboring entries in the delay matrix. The procedure for smoothness regularization of the delay matrix is explained in more detail in Appendix A. After regularization of the delay matrix the problem of outliers is solved, with as result a more plausible range of delay values. Shown are the regularized correlation and delay matrices (see Fig. 2, top right) that were obtained for 843 IEDs occurring in the first 24 h of the SEEG recording of patient 1. In order to compute the correlation matrix $\boldsymbol{h^2} = \left\{(h^2_{ij})_{\max,\text{regularized}}\right\}$ and the delay matrix $\boldsymbol{\tau} = \left\{(\tau_{ij})_{\max,\text{regularized}}\right\}$, it is necessary to evaluate both the combinations $i \to j$ and $j \to i$ since the correlation coefficient is asymmetric, i.e. $\bar{h}^2_{ij} \neq \bar{h}^2_{ji}$ (Pijn and Lopes da Silva, 1993).

2.5. Brain areas involved in the IEDs

To estimate the likeliness of a brain area to generate epileptiform activity, the GLM is applied, which is a generalized form of multiple regression analysis. The GLM is used to model the statistical relation between the occurrence of the IEDs and the associated time-varying correlation of the SEEG signals. This approach is based on the assumption that mutual correlations between electrodes increase during epileptiform activity (Bettus et al., 2008). The univariate GLM is evaluated for all pairs i and j and is formulated as follows

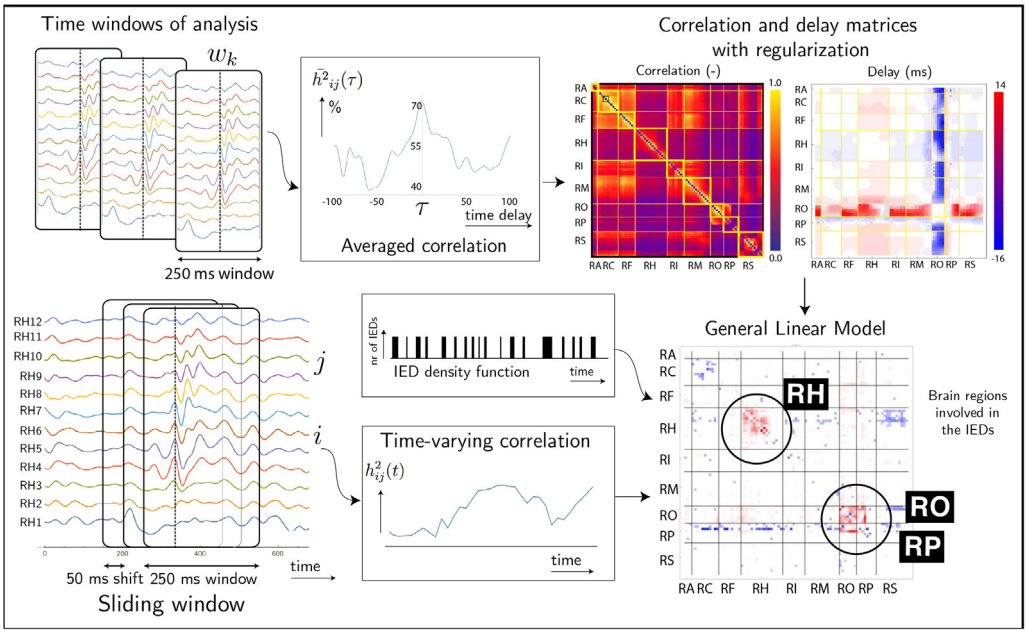

Fig. 2. Overview of the analysis applied to the SEEG recordings of patient 1, as indicated in steps 1 and 2 of the flowchart for SEEG analysis (see Fig. 1). Top row: The non-linear correlation is computed for windows centered around the maximum of IEDs, shown by the vertical dotted line (left), from which the time delay can be estimated (middle) and summarized in correlation and time delay matrices (right). Shown in the middle is the averaged correlation as function of the estimated time delay. Bottom row: A sliding window analysis is performed (left) in which the changes in non-linear correlation over time are computed (middle). These time-varying correlation functions are together with the IED density function the input of the General Linear Model (GLM). The result of the GLM analysis reveals at which contact points SEEG signals are recorded that are significantly involved in the IEDs (right).

$$h^2_{ij}(t) = \beta_{ij}\mathrm{IED}(t) + \alpha_{ij} + \gamma_{ij}t + \eta_{ij}\mathrm{CONF}(t) + \epsilon(t), \tag{4}$$

where $h^2_{ij}(t)$ is the dependent variable describing the time-varying correlation. The time-varying changes in the correlation $h^2_{ij}(t)$ are computed using the sliding window approach, in which the correlation is estimated by overlapping time windows with a length of 250 ms and a sliding step of 50 ms (Fig. 2, bottom left). At a 600 Hz sampling rate, these windows correspond to 150 and 30 samples, respectively. The current study expands upon the GLM analysis for SEEG, introduced by van Houdt et al. (2012), by taking the delay estimation into account. In order to achieve optimal values in time-varying correlation $h^2_{ij}(t)$, in the current study a correction for the time delay is applied to each combination $i, j = 1, \ldots, \#_{\text{contacts}}$ according to the delay matrix computed for the considered patient. Formally the time-varying correlation is computed according to

$$h^2_{ij}(t) = h^2_{ij}\Big(w(t), (\tau_{ij})_{\text{max,regularized}}\Big) \tag{5}$$

where $w(t)$ is the sliding window centered around time t.

The correlation function is modeled by a linear combination of independent variables (i.e. regressors). The predictor of interest is the IED density function (Fig. 2, bottom middle) denoted by $\mathrm{IED}(t)$, obtained by counting the number of IEDs that occur throughout the SEEG recording selected for analysis. The other independent variables are confounding variables: a constant α, a linear trend β, and the confounder density function $\mathrm{CONF}(t)$. The model residual is given by $\epsilon(t)$. Artifacts that may occur in the EEG are included in the confounder density function $\mathrm{CONF}(t)$, which counts the number of artifacts that occur during the sliding window.

The GLM is expected to yield high regression coefficients β_{ij} for contact points that are highly synchronized during the occurrence of IEDs. After the initial estimation of the matrix of regression coefficients $\boldsymbol{\beta} = \{\beta_{ij}\}$, several procedures are employed to distinguish epileptically active regions from false positive regions. First, the $\boldsymbol{\beta}$-matrix is thresholded according to a significance level in order to reduce false positives. The p-values obtained from the GLM procedure are adjusted according to the false discovery rate (FDR) (Yekutieli and Benjamini, 1999) to correct for multiple testing, with every entry of the $\boldsymbol{\beta}$-matrix thresholded at $q < 0.01$. In extension to the method as introduced by van Houdt et al. (2013), a symmetry requirement on the regression coefficient is imposed, since synchronization during the occurrences of IEDs is expected to occur in both directions, i.e. $\beta_{ij} \approx \beta_{ji}$. Non-symmetric matrix elements can indicate the presence of an artifact. In order to remove the non-symmetric part of the $\boldsymbol{\beta}$-matrix, entries for which the condition $|[\mathrm{asym}(\boldsymbol{\beta})]_{ij}| = \left|\frac{1}{2}(\beta_{ij} - \beta_{ji})\right| > \frac{1}{2}\sigma$ holds are removed, where σ is the standard deviation of the distribution of significant $\boldsymbol{\beta}$-matrix values. Lastly, a selection of the highest $\boldsymbol{\beta}$-matrix values is done in order to select the most likely regions of focal activity. To select a suitable threshold, Otsu's method (Otsu, 1979) is applied, which is based on the estimation of Gaussian distributions in the $\boldsymbol{\beta}$-matrix histogram. The final $\boldsymbol{\beta}$-matrix is shown in Fig. 2 (bottom right), indicating for the example patient two distinct anatomical regions (encircled in black) targeted by three electrodes (RO, RP and RH). In conclusion, the GLM reduces the number of signals to be analyzed and thereby facilitates further analysis.

2.6. Interdependency assessment

In order to evaluate the interdependency of the brain areas involved in IEDs, ICA is applied to create spatial distributions of each individual IED, followed by hierarchical clustering to identify spike clusters that have similar underlying spatiotemporal interactions. Proposed by Jutten and Herault (1991), ICA is a statistical model where observed data is represented by a weighted sum of estimated source signals. This is expressed by $\vec{y}(t) = W\vec{x}(t)$ where $\vec{x}(t)$ is the observed data, $\vec{y}(t)$ are the estimated independent components and W is the unmixing matrix. Numerous variations of ICA

are available and have been used in the context of EEG analysis (Lipping et al., 2003; da Silva Braga et al., 2014). The current study employs the InfoMax ICA decomposition introduced by Makeig et al. (1997), which is a commonly used algorithm available in signal processing toolboxes such as EEGLab (Delorme and Makeig, 2004). A first requirement for Infomax ICA is that the sources must be statistically independent of each other, which is fulfilled when the sources have a low mutual information. The measure of statistical independence is the mechanism for source decomposition used by InfoMax ICA. The second requirement is that the observed data is stationary and not normally distributed. The EEG signals fulfill these requirements, since EEG is quasi-stationary, i.e. it is stationary within short time intervals during normal brain activity (Sanei and Chambers, 2007), while it is assumed that the EEG activity is not normally distributed.

InfoMax ICA is applied for each individual IED (Fig. 3, top left) thus generating a corresponding spatial weighting distribution W (Fig. 3, top right). The spatial weighting distribution provides a footprint of each individual IED, which can subsequently be clustered to identify groups of IEDs and investigate whether independent focal areas can be identified. To this end, Ward's method is applied (Ward, 1963), which is a general agglomerative hierarchical clustering procedure that merges clusters at each step based on a distance metric. The Frobenius norm of the matrix W, given by $\|W\|_F \equiv \sqrt{\sum_{i=1}^{m}\sum_{j=1}^{n}|W_{ij}|^2}$, is the distance metric used in order to cluster the spatial distributions. Since the most interesting information is contained within the first few independent components, the latter containing mostly noise, the distance metric is only calculated on the first 10 components of the weighting matrices. An average of the IEDs and the spatial distribution of the independent components of these discharges is shown in Fig. 3 (bottom left). The hierarchical clustering is based on the similarity of the spatial distributions of the independent components of the individual IEDs. The number of clusters that can be discriminated as output of the clustering procedure can be estimated based on a dendrogram (Fig. 3, bottom row).

In order to estimate the number of clusters quantitatively, the gap statistic (Tibshirani et al., 2001) is employed. The gap statistic compares the clustering of SEEG recordings against a second clustering result of a randomly generated dataset of the same dimensions and the same range of values. The gap statistic compares the within-cluster dispersion between both clustering results, which is a measure of the average distance between the elements within all clusters. The within-cluster dispersion is expected to become lower as the number of clusters increases, since elements within a cluster are increasingly alike. The difference between within-cluster dispersion measured in both datasets forms the gap statistic. Based on the gap statistics two well-separated spike clusters that differ in spatiotemporal distribution, i.e. the shape of the IEDs and the anatomical area at which these discharges are maximal can be distinguished (Fig. 3, bottom row, right). More details on the gap statistic applied to hierarchical clustering can be found in Tibshirani et al. (2001).

In some cases the gap statistic can be inconclusive. In those cases, an alternative approach to estimate the number of clusters is used. In this approach the number of clusters is manually estimated based on the expected number of independent focal areas. The intermediate results are then clustered for a second time using a K-means algorithm to discover groups of similar clusters or deviating clusters. Again, Otsu's method (Otsu, 1979) is applied, but now for selecting the contact points of electrodes with the highest response by considering the accumulated weighting of the first 10 components.

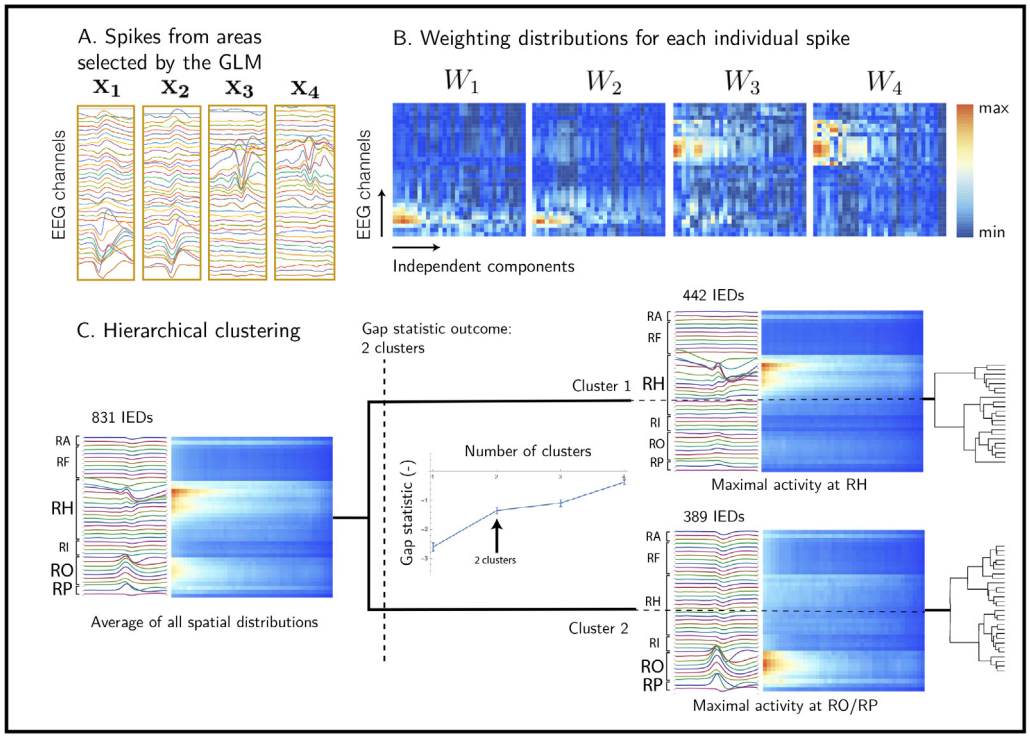

Fig. 3. Overview of the clustering procedure to assess the interdependency of focal brain areas applied for patient 1, as indicated in steps 3 and 4 of the flowchart of the SEEG analysis procedure (see Fig. 1). ICA is applied for each spike individually (A), resulting in a spatial distribution matrix W for each spike (B). Shown at the bottom left is the average of all IEDs selected for further analysis and of their spatial distributions. Hierarchical clustering is applied to the set of individual spatial distributions, which results in a dendrogram (C). The gap statistic (Tibshirani et al., 2001) is used to estimate the number of clusters, indicating two spike clusters for this patient. The corresponding averaged spatial distributions for each cluster are shown, displaying a clear separation of the epileptic activity at either the electrode RH or at the crossing of the tips of the electrodes RO/RP.

Visualization

To visualize the brain areas and their interactions, an in-house developed depth electrode navigation software tool is employed. This tool provides automatic detection of depth electrodes and can visualize these electrodes on top of the underlying anatomy (Meesters et al., 2014). The spatial distribution of the activity underlying the IEDs recorded with the depth electrodes is visualized in a 2D- and 3D-viewport against pre-implantation MRI or against the cortical rendering (see for example Figs. 4–7). Furthermore, a model of the underlying interactions of the brain areas is visualized by the use of arrows, given with the estimated delay and indicating whether the brain areas are lagging or leading. In addition, each arrow corresponds to the depicted associated correlation, which is a measure of coupling strength.

3. Results

To evaluate the analysis framework the SEEG recordings were analyzed retrospectively for five patients (patients 1–5) who all underwent successful epilepsy surgery (Engel class 1&2). Furthermore, it will be shown that the network analysis approach developed in this study is successful for the patients included with a focal partial epilepsy, who were not seizure free after surgery (patient 6 and 7, Engel class 3&4). The results, as summarized for the seven patients in Table 2, are evaluated against the electroclinical hypotheses, the SOZ, the resected area and the surgical outcome. Furthermore, the activation patterns underlying the IEDs are displayed at the depth electrodes in relation to the brain anatomy for each of the seven patients studied.

3.1. Evaluation of the analysis framework

The analysis framework was evaluated for the five patients with disrupted anatomy visible at MRI (see Table 1, column 3) who underwent successful surgery. Patient 1 had a right frontal porencephalic cyst from birth with partial involvement of the right insular and temporal regions. For this patient, nine electrodes were implanted in the right hemisphere, targeting the hippocampus, temporal operculum, insula, cingulum, frontal and occipital lobes, and the area surrounding the patient's porencephalic cyst (Fig. 4, bottom left). The contact points at which the IED activity was maximal according to visual review are listed in column 3 of Table 2. These results can be compared to the quantified maximal IED activity as determined by the result of the analysis framework (Table 2, column 4). For this patient there are two spike clusters active, one in the right hippocampus (electrode RH) and one at the site of the right insula, at the crossing of the RO and RP electrode (Fig. 4, right top row). The spatial distribution of the individual clusters is displayed color-coded at the corresponding electrodes in a sagittal and axial MR scan (Fig. 4, right bottom row). The spike cluster that is maximal at the right hippocampus coincides with the SOZ as indicated by the yellow box in the sagittal MRI scan. The overlap as indicated in column 6 of Table 2 is computed by the intersection of: (1) the set of contact points identified by quantified IED activity, and (2) the set of contact points that correspond to the SOZ according to clinical review. The overlap is normalized by the number of contact points corresponding to the SOZ. For the first cluster, the overlap between the quantified IED activity and the SOZ is measured at 75%, indicating a good concordance. The second cluster involving the RO and RP electrodes targeting the right insula showed no overlap with the SOZ. The patient underwent a right anterior temporal lobe resection and amygdalohippocampectomy, which led to satisfactory seizure reduction.

In Fig. 5 an overview is given of the analysis results for patients 2, 3 and 4. The semiology of patient 2 indicated left temporal lobe epilepsy. The question when planning the implantation of the depth electrodes was whether the left hippocampus was involved in seizure generation and whether there could be an epileptogenic area related to the MRI abnormalities due to an earlier infarction at the left occipital lobe. Five depth electrodes were implanted in the left occipital lobe and a single depth electrode was implanted in the left hippocampus (Fig. 5A, left). The EEG signals that were, according to the GLM, significantly involved in the IEDs were mainly recorded with the electrodes LH, LB and LM. However, after ICA and subsequent spike clustering, a single spike cluster could be identified with a maximum at electrode LH (Fig. 5A, middle). The maximum, centered around LH5, coincided with the SOZ, as indicated by the yellow box in the sagittal MR scan (Fig. 5A, right). The overlap between the quantified IEDs and the SOZ is 45% (see Table 2, column 6). The patient was rendered seizure-free after a standard left temporal lobe resection and

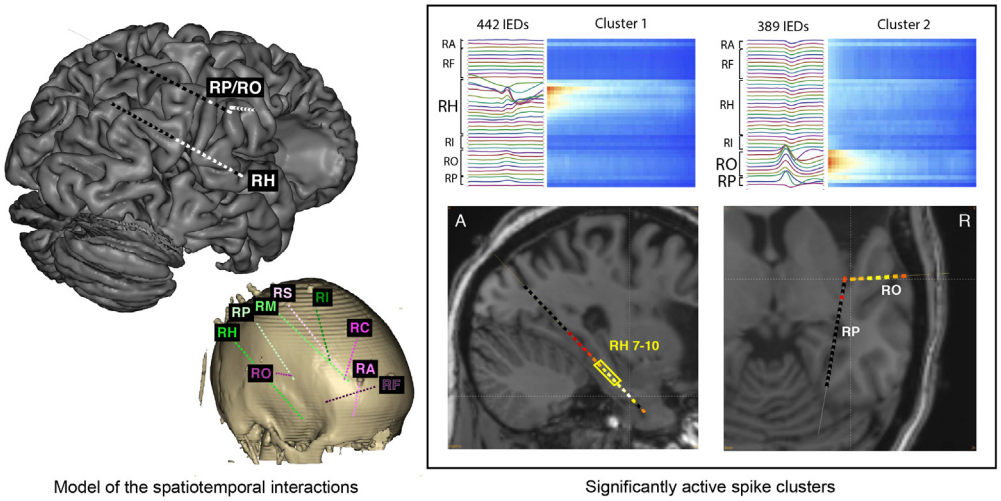

Fig. 4. The results of the SEEG analysis for patient 1, indicating the spatiotemporal pattern of the two spike clusters (upper right) and visualizing the significant activation at the electrodes RH, RO and RP (bottom right). The yellow box indicates the overlap of the activity underlying the IEDs and the SOZ. The model of the spatiotemporal interactions (top left) displays the electrodes with significantly involved activity underlying the IEDs indicated by the white dots. The nine electrodes implanted for this patient are displayed together with the 3D-CT scan of the patient's head (bottom left). (For interpretation of the references to colour in this figure legend, the reader is referred to the web version of this article.)

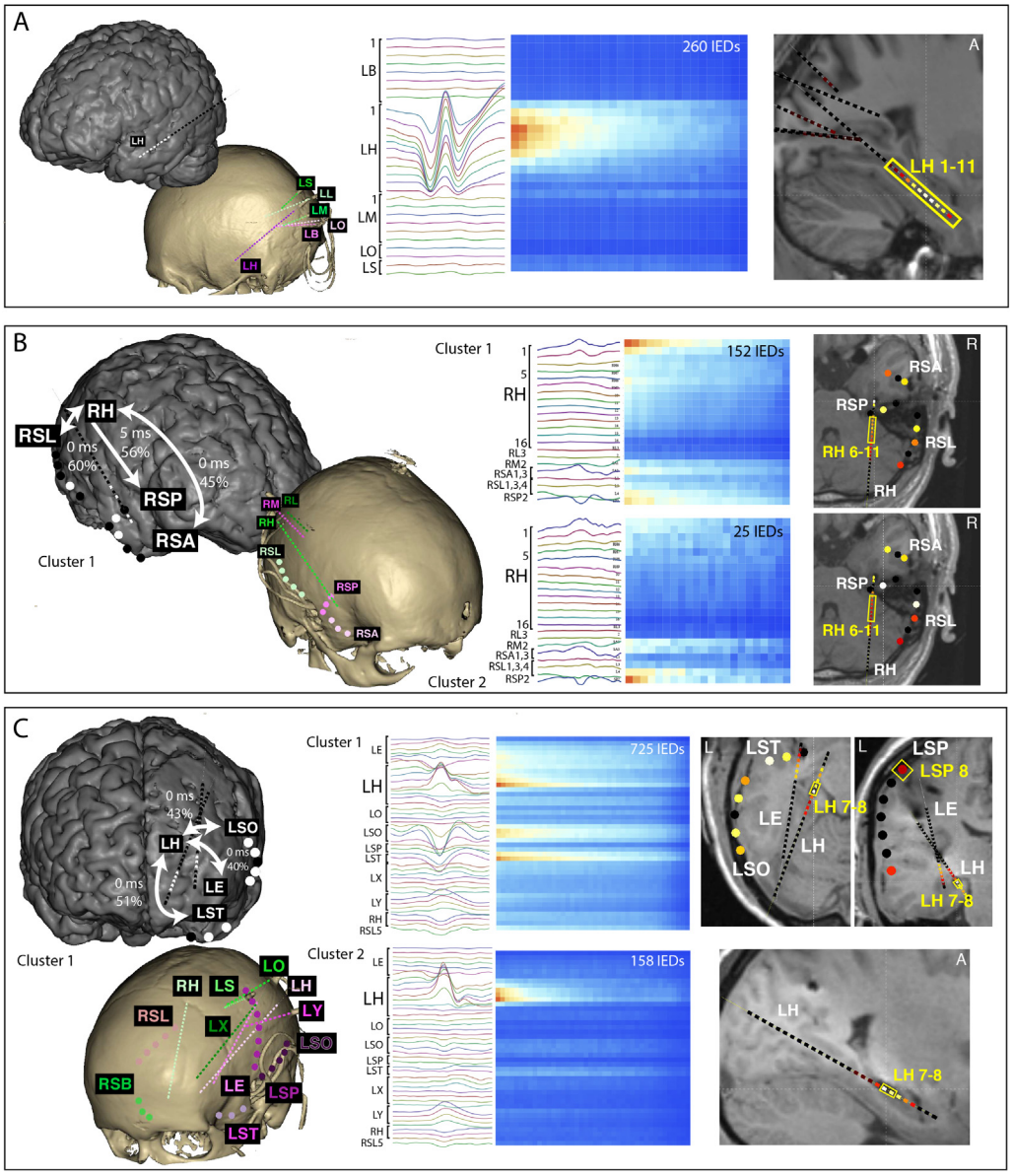

Fig. 5. Results of the SEEG analysis for patients 2 (A), 3 (B) and 4 (C). In the left column the implanted electrodes are shown together with the 3D-CT scan and the spatiotemporal model of the interactions underlying the IEDs. The middle column shows the output of Independent Component Analysis followed by hierarchical clustering, indicating the number of spike clusters and their spatiotemporal patterns. In the right column, the activity corresponding to these spike clusters is projected on anatomical MRI slices with the location of the SOZ indicated by the yellow box. (For interpretation of the references to colour in this figure legend, the reader is referred to the web version of this article.)

amygdalohippocampectomy. For patient 3, three depth electrodes were implanted in the right temporal and occipital lobes (RH, RC, RI). Furthermore, three subdural strip electrodes were placed (Fig. 5B, left) in the right anterior basal temporal (RSA), posterior basal temporal (RSP) and lateral temporal regions (RSL). According to the GLM the EEG signals recorded with electrodes RH, RSA, RSL and RSP were significantly involved in the IEDs. ICA with subsequent cluster analysis yielded two spike clusters (Fig. 5B, middle), which was supported by the gap statistics. The spike cluster shown at the top row is dominant at electrode RH, whereas the second spike cluster shown at the bottom row is dominant at the subdural strip RSP. Note that the spikes recorded at the subdural RSP strip are inversed in polarity because of the placement of the RSP strip posterior basal to the hippocampal electrode. The most significant activity is recorded at the tip of the RH-electrode, however, the SOZ is located more posterior in the right hippocampus (see the yellow box in Fig. 5B, right, top row). The overlap between the quantified IEDs and the SOZ is 50% (see Table 2, column 6). A right anterior temporal lobe resection and amygdalohippocampectomy led to a satisfactory seizure reduction.

The recordings of patient 4 (Fig. 5C) reflected large IEDs at the left temporal and left occipital lobes. For this patient seven depth electrodes were implanted in brain areas including the left and right hippocampus (LH and RH), left insula (LX, LY) and left parietal (LE, LO, LS) lobes. In addition, five subdural strip electrodes were implanted in the right basal (RSB) and lateral temporal (RSL) regions, the left anterior basal temporal lobe (LST), left temporo-occipital (LSO) and parietal lobes (LSP). According to the GLM, EEG signals measured with the electrodes LH, RH, LX, LY, LSO, LST, and RSL were significantly involved in the IEDs. However, after ICA, together with hierarchical clustering, two clearly distinct spike clusters were obtained that were both dominated by activity at the

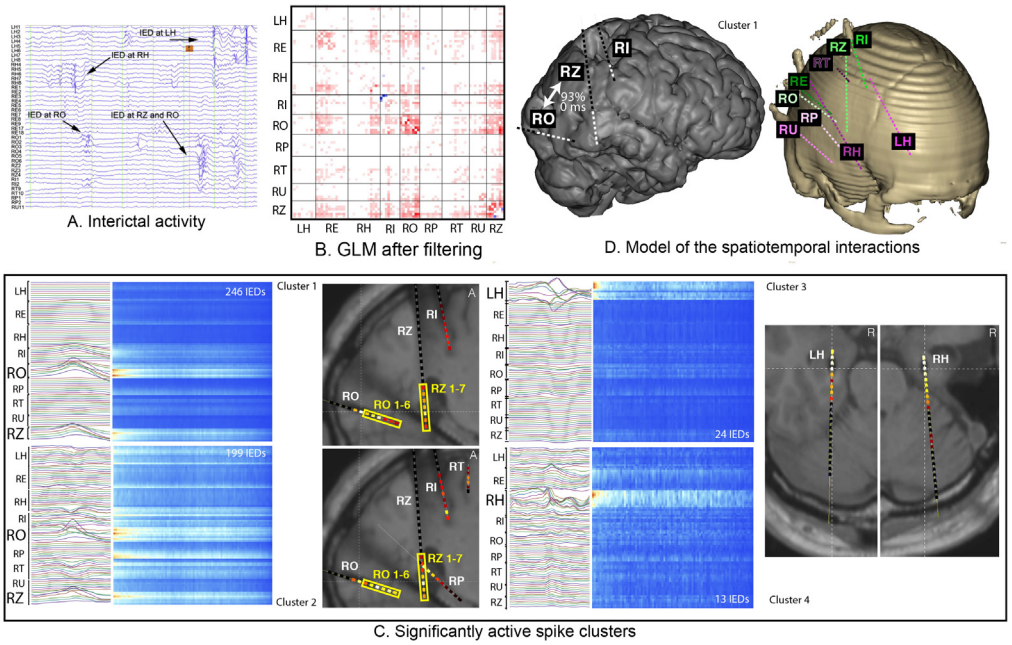

Fig. 6. Results of the SEEG analysis for patient 5. (A) The SEEG recording showing IEDs at the depth electrodes. (B) The output of the General Linear Model indicating that most of the SEEG signals are significantly involved in the epileptic discharges. (C) The spatiotemporal distribution of the distinct spike clusters involved. At the left, the spike clusters are shown with maximal activity at electrodes RO and RZ. The overlap with the SOZ is indicated by the yellow boxes. At the right, the spike clusters with maximal activity at, respectively, the electrodes targeting the left (LH) and right (RH) hippocampus. (D) The model of the network organization which shows the depth electrodes that are part of the epileptic network (left). The association strength ratios are denoted in percentages and the estimated delays are given in milliseconds. The implanted depth electrodes are shown together with the CT-scan at the right.

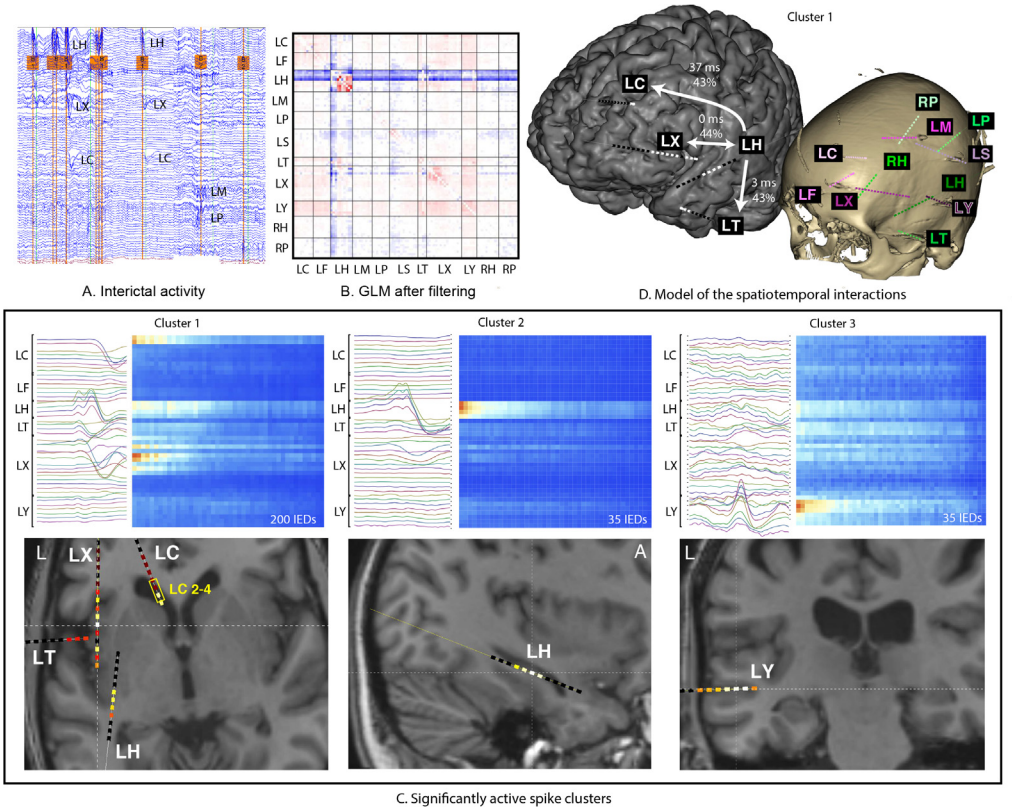

Fig. 7. Results of the SEEG analysis for patient 6. (A) The SEEG recording showing the IEDs at a selection of depth electrodes. (B) The output of the General Linear Model displaying which SEEG signals are significantly involved in the epileptic network. Positive β values (red) indicate increased correlation during IEDs, while the negative β values indicate a decorrelation during IEDs. (C) The three distinct spike clusters with the complete network involved (left), dominant activity at electrode LH (middle) or dominant activity at the electrodes LY/LX (right). (D) The model of the spatiotemporal interactions underlying spike cluster 1 (left) and the implanted electrodes visualized relative to the 3D-CT scan (right). (For interpretation of the references to colour in this figure legend, the reader is referred to the web version of this article.)

electrodes located at the left temporal lobe (Fig. 5C, middle). Cluster 1 reflects simultaneous activity from LH and LSO mainly and with a smaller amplitude LST, while for cluster 2 the activity recorded with the LH electrode dominates. The left hippocampus targeted by the LH electrode coincides with the SOZ (Fig. 5C, right) showing a 67% overlap (see Table 2, column 6). For this patient, a left extended temporal lobe resection and amygdalohippocampectomy was performed rendering this patient seizure-free.

Patient 5 had a cystic lesion due to a perinatal infarction in the temporo-occipital lobe of the right hemisphere. Eight depth electrodes were implanted adjacent to the infarction, with in addition one electrode implanted in each the left and right hippocampus (Fig. 6D, right). The GLM reflects a diffuse pattern, indicating significant activity measured by all electrodes (Fig. 6B). Therefore, no electrodes were excluded from further analysis. ICA was applied followed by hierarchical clustering. The interactive method was employed for estimating the number of clusters since the gap statistic was inconclusive. Cluster 1 is mainly dominated by activity recorded at several contact points of RO and RZ, whereas cluster 2 reflects more diffuse activity with involvement apart from the activity at RO and RZ of the electrodes LH, RI, RP and RT, albeit of lower intensity. Further visual review indicated that for cluster 1 the activity dominated alternately at electrode RO and RZ, whereas cluster 2 mainly reflects distributed activity over six of the implanted electrodes. The clustering results of this patient reveal in addition two spike clusters, with dominant activity at both the left and right hippocampal electrodes (Fig. 6C, right). These clusters consist of, respectively, 24 and 13 IEDs, amounting to less than 5% of the total number of IEDs occurring in the selected SEEG recordings of this patient. It appeared that the pathological brain area targeted by the electrodes RO and RZ coincided with the SOZ, as indicated by the yellow boxes at Fig. 6C, with an overlap of 90% (see Table 2, column 6). An extended resection of the brain area including the cystic lesion was performed rendering this patient seizure-free.

3.2. Network analysis approach

A network underlying the IEDs is assumed to consist of nodes, which are the brain areas involved in the evolvement of the IEDs, and the connections between these nodes. The connections are expressed by the association strength (correlation value $\times$ 100 %), while the estimated time delay (in ms) indicates the direction, i.e. whether the node is leading or lagging. The scope of the network analysis procedure was, however, limited for the five patients who participated in the evaluation study because the implantation strategy of the depth electrodes was mainly guided by the abnormalities visible at MRI. The two spike clusters of patient 1, located adjacent to the porencephalic cyst and probably originating in the right hippocampus and insular area, were independently active. For patient 2 a single spike cluster was identified with an origin in the left hippocampus. The spatiotemporal interactions of the spike clusters identified for both patient 3 and 4 are restricted to, respectively, the right and left temporal lobe (see Fig. 5B,C). For these patients there was a negligible time delay between the spikes recorded at the hippocampal electrodes and the subdural electrode strips. Thus, the SOZ of 4 out of 5 patients evaluated (patient 1–4) originated in either the left or right hippocampus and a standard or more extended temporal lobe resection plus amygdalohippocampectomy led for each of these patients to a satisfactory seizure outcome. The SEEG recordings with the most complex interactions of the MRI-positive epilepsy patients were recorded for patient 5 (Fig. 6A). Spike clusters with the most dominant activity were identified at the RO and RZ electrodes with varying spike amplitude but without significant time delay between these electrodes. Furthermore, the electrodes placed in the left and right hippocampus revealed independent interictal spiking (Fig. 5C), but did not interact with the RO and RZ electrodes. In summary, there is no evidence for interactions with distant brain areas for the 5 patients included in the evaluation study with an epilepsy related to pathologic brain tissue identified at MRI.

The network analysis approach appeared, especially, suitable for patients who had, according to visual review, an epilepsy with underlying complex network interactions. For one of the two patients studied (patient 6), who was not seizure free after SEEG guided resections, electro-clinical review indicated focal partial seizures with secondary generalization. Visual review of the SEEG recordings pointed at a neocortical left temporal lobe epilepsy, possibly with involvement of the contralateral temporo-parietal regions. For this patient, in total nine electrodes were implanted in the left hemisphere and two electrodes were implanted in the right hemisphere, including a depth electrode in each of the hippocampi (Fig. 7D, right). Visual analysis of seizure data identified the left anterior cingulum targeted by depth electrode LC as the SOZ. However, the patient was not seizure-free after resection of this area. The SEEG recordings of this patient mainly reflect IEDs recorded at the depth electrodes implanted in the left frontal and temporal lobes (Fig. 7A). GLM analysis (Fig. 7C) revealed significant activity measured from six depth electrodes (LH, LX, LC, LF, LY and LT). Subsequently, ICA followed by hierarchical clustering yielded three spike clusters (Fig. 7C, upper row) with involvement mainly of five electrodes (LH, LC, LY, LX and LT). Spike cluster 1 reflects the interaction of the activity underlying the discharges recorded at the electrode targeting the left hippocampus (LH), which is leading the activity recorded, respectively, at the electrodes targeting the left temporal pole (LT), anterior insula (LX) and anterior cingulum (LC). Spike cluster 2 is mainly recorded at the electrode targeting the left hippocampus and its direct neighborhood, while the third spike cluster was maximal at the LY electrode targeting the left insula. The interactions between brain areas for cluster 1 are visualized in (Fig. 7D) in which the delay values are depicted, showing the LH-LX electrodes as the focal area with propagation towards the other electrodes, with small delays towards LY and LT and larger delays to LC and LF. The network interactions as identified by the analysis framework applied in this study all point to the left hippocampus as being responsible for the initiation of the IEDs of this patient. The interictal activity (quantified) is not concordant with the clinical hypothesis regarding the SOZ and has 0% overlap (see Table 2, column 6).

Patient 7 was diagnosed with an epilepsy of unknown origin with secondary generalization and with either a left, right or bilateral frontal onset. For this patient, 9 electrodes were implanted in the right hemisphere and 6 in the left hemisphere (Fig. 8D). GLM analysis indicated significant activity measured mainly from LC, LX, RA, RC, RX and RY (Fig. 8B). ICA followed by hierarchical clustering yielded three spike clusters (Fig. 8C, upper row). All clusters indicate IEDs with high amplitude arising from the right insula (RY). Furthermore, all clusters indicate activity from the left and right insular and cingulate regions. The depth electrodes implanted in the left and right insular areas (LX, RX and RY) and area of the cinguli (LC, RA and RC) were interictally active. According to the clinical hypothesis based on these depth electrode recordings the SOZ was located in the area of the right middle frontal gyrus. However, resection of this area did not lead to a satisfactory seizure reduction.

Delay estimation by the regularization procedure did not lead to plausible results for this patient, showing mostly delays estimated around 0 ms, likely due to the varying shape of the IEDs within each spike cluster. In order to resolve these issues, a local maximum based analysis of the correlation function given by Eq. (2)

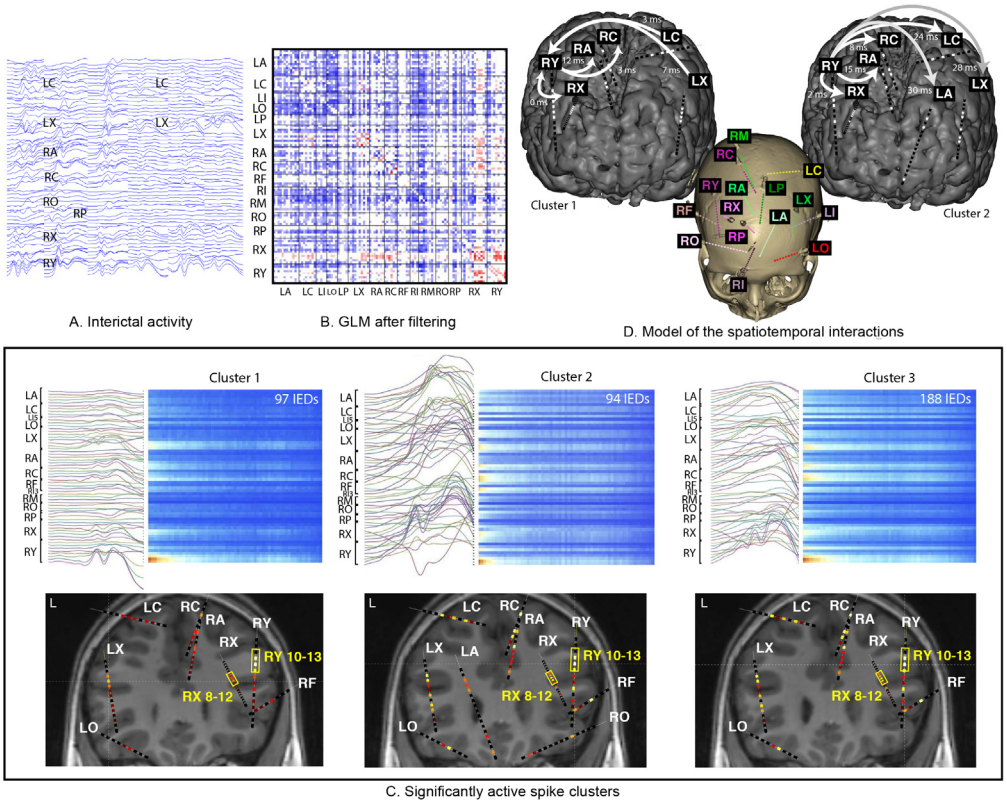

Fig. 8. Results of the SEEG analysis for patient 7. (A) The SEEG recording showing the IEDs at different depth electrodes. (B) The output of the General Linear Model displaying which SEEG signals are significantly involved in the epileptic network. Positive β values (red) indicate increased correlation during IEDs, while the negative β values indicate a decorrelation during IEDs. (C) Independent Component Analysis followed by hierarchical clustering indicates three spike clusters. All spikes clusters display complex activity involving multiple involved electrodes. (D) The model of the network organization showing that the activity recorded at LX is leading for cluster 1 (left) and the activity recorded at electrode RY for cluster 2 (right). The implanted electrodes are displayed relative to the 3D-CT scan (middle). (For interpretation of the references to colour in this figure legend, the reader is referred to the web version of this article.)

is performed. Details of this additional procedure are given in Appendix B. The first cluster shows that activity from the left insula and cingulum precedes the activity seen in the right hemisphere (Fig. 8C, left). The second cluster indicates the right hemisphere as a clear onset region, showing large delays up to 30 ms to the left cingulum (Fig. 8C, middle), but indicates simultaneous activation of the sources targeted by LX and RY, but also including LC and RC. The third cluster appears to be a mixture of clusters 1 and 2, showing distributed activity originating from both the left and the right hemisphere (Fig. 8C, right). In conclusion, the results of the analysis framework indicate that the most dominant IEDs of this patient, both in number and amplitude, are initiated in the right middle frontal gyrus and right anterior insula. However, the activity originating in the left middle frontal gyrus and left anterior insula also contributes to the IEDs of this patient. Furthermore, as result of the network analysis approach it appears that the electrodes in the left middle frontal gyrus and left anterior insula are leading in cluster 1, while cluster 2 shows that electrodes from the right middle frontal gyrus and right anterior insula are leading. For cluster 2, concordance of the focal areas identified in the right hemisphere, at electrodes RX and RY, and the SOZ is measured at 56% (see Table 2, column 6). Evidently, the focal area identified by cluster 1 at electrodes LX and LC did not overlap with the SOZ as identified by visual review of the SEEG recordings. After surgical intervention of the right middle frontal gyrus the seizures started to reoccur, but now clearly with a left hemispheric origin, thus indicating that surgical intervention was successful for the seizures arising from the right hemisphere.

4. Discussion

A framework developed to map the spatiotemporal interactions of interictal stereo-EEG was evaluated, retrospectively, for the depth electrode recordings of epilepsy surgery candidates (N = 7). For five of these patients who underwent successful surgery it was investigated whether multiple focal brain areas were interacting. Furthermore, the leading brain area was identified and related to the electro-clinical hypotheses with regard to the SOZ. The additional value of the analysis framework was further demonstrated by the presentation of the results for two patients with complex network interactions underlying their IEDs. These patients had no satisfactory seizure outcome despite long term SEEG recordings guiding their surgery. The analysis framework applied to the SEEG recordings of these two patients yielded spike clusters originating, according to the network analysis approach, in leading brain areas, which did not coincide with the resected area. The results presented here provide evidence that for these patients systematic network analysis of the activity underlying the IEDs would have been of importance in addition to routine review of SEEG recordings to guide resective surgery.

4.1. Methodology: limitations and improvements

In order to study the couplings and time delays between SEEG signals during the occurrence of IEDs non-linear correlation analysis was applied. Contrary to the commonly used method (see e.g.

Wendling et al. (2001a), van Houdt et al. (2012)) the time delay estimation is based on the average correlation function of a large number of IEDs. In the current study a matrix representation is used for the correlation and time delay estimates in order 1) to avoid errors due to highly varying correlation values at distinct contact points of a particular electrode, and 2) to enable regularization of the delay estimations. The newly introduced regularization procedure led to a delay matrix that contains fewer outliers and reflects a range of delay values that is within a more plausible range based on physiological expectations. In case of high variability of the interictal spike activity, like for patient 7, the delay estimation appears to be inaccurate despite regularization. Therefore, an alternative approach for delay estimation was introduced, which diminishes the influence of IEDs of deviating shape, resulting in a more accurate delay estimation for this patient. The non-linear correlation coefficient h^2 together with the regularization procedure provides a robust method to estimate delays. However, non-linear multivariate regression methods, such as generalized synchronization (GS) or phase synchronization (PS) (Pereda et al., 2005), might be possible alternatives, although these methods were not applied yet to the extent of our knowledge for SEEG signal analysis.

The current study adopts and extends the use of the GLM approach firstly introduced by van Houdt et al. (2012) for the purpose of the identification of these brain areas that generate highly synchronized activity during the occurrence of the IEDs. The application of the GLM is a crucial step preceding ICA based on individual IEDs, because it reduces the number of signals to be analyzed, leading to better modeling outcomes and significantly reduced computation time. The outcome of the GLM is represented in a β-matrix, which, as opposed to the approach by van Houdt et al. (2012), does not require the averaging of the time-varying correlation of multiple depth electrode signals. Non-significant and artifactual matrix entries could in most cases be removed successfully from the β-matrix through statistical significance testing and through symmetry filtering. Correcting for multiple comparisons through the FDR method effectively imposes stricter requirements on the p-value, which, especially for large matrices, is important to reduce false positives. Imposing a requirement on symmetry was effective in reducing outliers in the β-matrix. However, if it is not possible to reduce the number of SEEG signals, as was the case for patient 5, for whom the results are presented in Fig. 6B, a high number of multicolinear variables remain, which have an adverse effect on the performance of ICA because 1) an artifactual source present in the EEG may be spread out over multiple components, and 2) a single SEEG signal is representing multiple components. A possible solution is to apply principal component analysis (PCA) as a dimension reduction step before applying ICA (Hyvarinen and Oja, 2000). An unexpected outcome of the GLM was that its results reflect negative values for several patients, which were retained regardless of the filtering procedure based on FDR-adjusted p-values or by imposing a symmetry requirement. Negative β-values might be the result of sudden unexplained discharges or changes of the SEEG signals that could not be adequately compensated for by the confounder density function. Overall, the GLM has proven to be useful for selecting the brain areas that generate the highly synchronized activity underlying the IEDs.

The application of ICA followed by hierarchical clustering appeared to be an effective method for identifying spike clusters with a distinct spatiotemporal pattern. The clustering of spatial distributions was inspired by Van 't Ent et al. (2003) who applied spike cluster analysis of IEDs occurring in the magnetoencephalogram (MEG). The foremost limitations of the hierarchical clustering method are that it may be unclear how many spike clusters should be selected, and, secondly, which of the selected clusters reflect focal activity. In the current study, the optimal number of clusters was quantitatively determined by the gap statistic. However, the optimal number of clusters may include, regardless of the restrictive statistics, clusters with a very low number of spikes, like for patient 5 with a spike cluster originating in the left and right hippocampus. The relevance of these spike clusters remains unclear, also because they were not interacting with the spike cluster which was concordant with the SOZ. The gap statistic did not produce a conclusive answer for patient 5 (see Fig. 6) and patient 6 (see Fig. 7) since the criterion for determining the number of clusters as described by Tibshirani et al. (2001) could not be met. For these cases it was possible to successfully use the interactive method described in Section 2.6 to estimate the number of clusters. In future work it should be investigated whether the use of advanced ICA models can yield sources with a greater statistical independence and therefore provide more robustness to noise. Examples of this type of advanced models are convolutive ICA (Dyrholm et al., 2007) or mean-field approaches (Højen-Sørensen et al., 2002), which incorporate reverberations and convolutive mixing, and may be more appropriate for dealing with SEEG data than the InfoMax algorithm as applied in the current study. A possible alternative to the approach of hierarchical clustering followed by the gap statistic is the robust growing neural gas network introduced by Qin and Suganthan (2004), which provides an outlier-resistant scheme and a cluster repulsion method for the removal of IEDs with an aberrant waveform, and furthermore allows for the automatic estimation of the number of clusters.

A network analysis approach was applied to characterize the spatiotemporal interactions of the network underlying the IEDs. The aim was to identify the leading or lagging nodes within the spatiotemporal network by the robust estimation of time delay to each spike cluster individually. The robust estimation of time delays between SEEG signals indicates the area of early onset of the IEDs, which coincides, according to the results presented for each of the patients studied, with the SOZ, and, furthermore, indicates the interaction of this area with brain areas involved in the network activity underlying the IEDs. Because of the complex nature of directionality estimation from SEEG recordings, averaging the spikes within a cluster, which reflect the same spatiotemporal interactions, can lead to an increased non-linear correlation coefficient (Pijn and Lopes da Silva, 1993) and thereby provide a more accurate estimate of the time delay. However, small time delays may occur, as was seen for patients 3–5, because the electrodes were positioned close together, which may require a higher SEEG sample rate than 600 Hz to determine the directionality. However, the identification of leading and lagging nodes of the network was shown to be successful for patient 6 (see Fig. 8C, left), for whom the activity underlying the first spike cluster stipulated that the mesiotemporal area precedes the cingulum and for patient 7, for whom independent focal areas were identified as being responsible for the three distinct spike clusters. In future work it should be assessed whether the potential of the directionality index, as introduced by Wendling et al. (2001a,b, 2010), in combination with the robust estimation of time delay as introduced in this study to unravel the leading and lagging of nodes of the network underlying IEDs could improve these results. A downside of any correlation-based technique is that a high correlation does not necessarily infer causation and information flow. Other methods, such as non-linear Granger causality, may provide a distinction between spurious information flow and true information exchange and, therefore, could possibly be more accurate at identifying the area of early onset of epileptic discharges. However, the limitation in our study are the short time windows used to analyse the IEDs (250 ms, or 150 data points at a sample frequency of 600 Hz). Due to the limited analysis epoch there may be insufficient statistical power for a reliable analysis using standard Granger causality. Variations such as the non-linear Kernel Granger causality (Marinazzo et al., 2011)

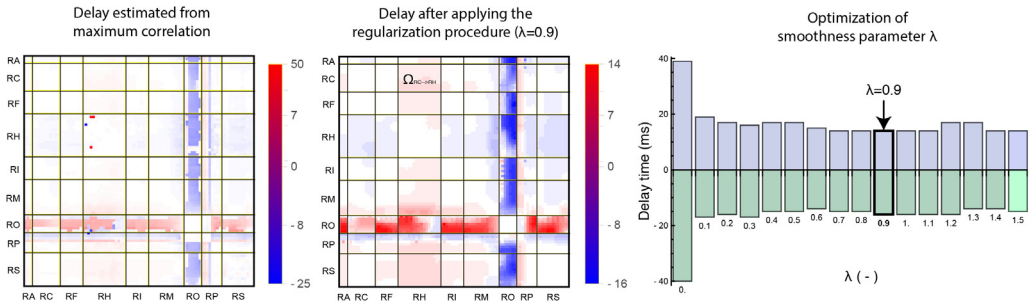

Fig. 9. Example of the regularization procedure for patient 1. Left: Delay matrix estimated from the estimation of maximum correlation. Middle: Delay matrix obtained after the regularization procedure. Right: Selection of an appropriate smoothness parameter λ through a stability analysis.

have been created to support relatively short signals, but are, as of date, unproven for SEEG analysis. Recently, it was shown by Bartolomei et al. (2017) that graph theoretical analysis of interictal SEEG recordings may provide us with a possible biomarker to identify abnormalities in the interictal network. In future work it should be assessed whether graph theoretical analysis as described by e.g. Bullmore and Sporns (2009) and Stam and van Straaten (2012) enables to describe the interactions of the distinct brain areas involved in the IEDs and whether it can improve the ability to pinpoint that area that is responsible for the epilepsy of the patient.

4.2. Clinical perspective

The first 24 h of SEEG recordings generally do not reflect any seizures, but may contain a large number of IEDs and can therefore provide an initial overview of the epileptic activity patterns related to the epilepsy of a patient. In practice this could lead to a reduction of the recording time needed.

However, an important prerequisite for analysis of these SEEG data using the framework of analysis as presented is the accurate annotation of IEDs. Considerable time and effort by a skilled EEG technician is required to annotate long-term SEEG recordings. It is, therefore, of utmost importance to proceed towards a (semi-) automatic framework for SEEG analysis through the automatic detection of IEDs.

A major limitation of any intracranial EEG-recording is the spatial resolution that can be achieved. For the five successfully operated patients the implantation strategy was mainly guided by the abnormalities visible at the MRI, which limits the network analysis approach. For example, for patient 1 (see Fig. 4) a relatively low number of electrodes were placed in the temporal lobe, thus limiting further investigation of interactions between the left hippocampus and insular cortex. Interactions between these regions would be expected based on the classification of network interactions reported on by Kahane and Bartolomei (2010). The same limitation of spatial sampling was seen for patient 2 (see Fig. 5A), for whom an electrode was targeting the left hippocampus, but there were no electrodes implanted in the left temporal lobe. However, the implantation of depth electrodes for the two failure patients was not guided by abnormalities visible on MRI. The epileptic events of these patients were characterized by rapid, and for one of the patients generalized, propagation of the activity underlying the IEDs. Therefore, the implantation of depth electrodes was much more widely distributed than for the 5 patients who had abnormalities visible at MRI. On basis of this hypothesis, the patients received a more distributed implantation of electrodes in both hemispheres. It was shown that for these patients with complex focal epilepsy, for whom seizures could not provide a conclusive clinical image, network analysis of IEDs is potentially a valuable tool to describe the spatiotemporal interactions of the epileptic discharges and to identify the SOZ. Overall, the approach as introduced in this study might increase the success rate of resective surgery, or could be helpful to select these patients who should be further investigated as candidates for alternative treatments.

5. Conclusion

A framework of analysis was developed to identify the network interactions underlying the IEDs occurring in SEEG recordings. The interdependency was assessed between brain areas that reflected highly synchronized neural activity. The time delay between nodes of the network was estimated by a new robust method and was used to map the spatiotemporal network interactions. The additional value of a network analysis became apparent, especially, for MRI-negative patients with a complex epilepsy. In conclusion, the analysis of IEDs by the analysis framework introduced in this study is considered a valuable addition to the routine review of SEEG recordings, with the potential to increase the success rate of epilepsy surgery.

Conflict of interest

None of the authors have potential conflicts of interest to be disclosed.

Acknowledgments

Funding was received as part of the Devices for NeuroControl and NeuroRehabilitation (DeNeCor) project from the ENIAC Joint Undertaking (Grant No. 324257) and as part of the Advancing Smart Optical Imaging and Sensing for Health (ASTONISH) project from the ECSEL Joint Undertaking (Grant No. 692470). The work of Andrea Fuster is part of the research programme of the Foundation for Fundamental Research on Matter (FOM), which is financially supported by the Netherlands Organisation for Scientific Research (NWO).

Appendix A. Regularization of the delay matrix

Details are provided of the regularization procedure for the reduction of outliers in the delay matrix. Since two neighboring SEEG contact points measure activity from an overlapping area, it is assumed that the correlation and associated estimated delay vary continuously between neighboring matrix entries. Based on this assumption, a smoothness constraint is implemented within the energy term used for regularization, formulated according to

$$E_{\Omega} = \sum_{(i,j)\in\Omega} \bar{h}_{ij}^{2}(\tau_{ij}^{*}) - \lambda\left|\Delta\tau_{ij}^{*}\right|, \tag{A.1}$$

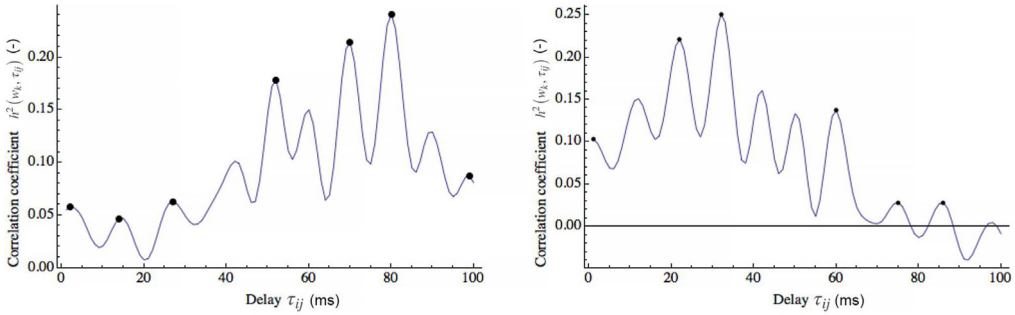

Fig. 10. Example outcome of the correlation profiles of $h^2_{ij}(w_k, \tau_{ij})$ (left) and its transpose $h^2_{ji}(w_k, \tau_{ij})$ (right). The local maxima are denoted by black dots. It can be observed that the local maxima are anti-symmetric around the origin $\tau = 0$.

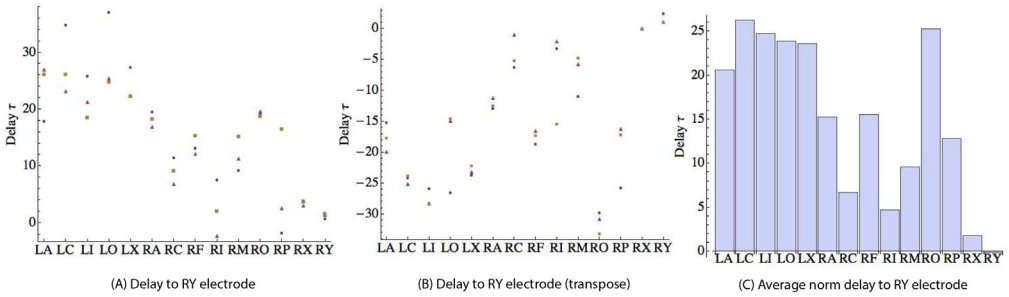

Fig. 11. Results of the delay computed from the weighted arithmetic mean of a set of delays weighted by their correlation value. The results for both sets τ_{IJ} (A) and τ_{JI} (B) are shown, displaying the approximately anti-symmetry property around the origin $\tau = 0$. The averaged norm of both delays $\tau_{I\leftrightarrow J}$ (C) displays that the EEG signals measured from electrodes implanted in the left hemisphere are lagging behind those in the right hemisphere.

where $\bar{h}^2_{ij}(\cdot)$ is the average correlation function (see Eq. (2)), τ^*_{ij} is the time delay value to be optimized at the indices for depth electrode signals (i,j), and λ is a weighting term for the degree of smoothness applied to the delay matrix. Here, Ω is an area of the delay matrix corresponding to the contact points of any two electrodes, for example containing the time delays from every signal measured by the RC electrode to every signal measured by the RH electrode (see Fig. 9, middle). Optimization is performed within Ω to ensure that the smoothness is evaluated in the same anatomical areas. The Laplace operator $\Delta = \nabla \cdot \nabla$ is used to measure the ariation between neighboring values in the delay matrix within Ω. In order to ensure smoothness to all neighboring values, a 9-connected discrete approximation of the two-dimensional Laplace operator is used. The nine-point Laplacian with stepsize h is given by $\Delta u = -h^{-2}[8u_{i,j} - u_{i-1,j} - u_{i+1,j} - u_{ij-1} - u_{ij+1} - u_{i-1j-1} - u_{i-1j+1} - u_{i+1j-1} - u_{i+1j+1}]$ (Lindeberg, 1994). We used stepsize $h = 1$.

The time delay τ^*_{ij} is optimized by maximizing the energy function E_Ω, which is done in a three-step procedure:

1. Initial values for the maximum correlation and the corresponding delay are computed for all entries in Ω based on the time-shifts that resulted in maximum correlation.
2. A direct search method is applied which optimizes each matrix entry (i,j) individually by computing the energy term for a range of delay values ($\pm$10 ms around τ^*_{ij}). The delay value corresponding to the highest energy is updated according to $\tau^*_{ij} = \left(\tau^*_{ij}\right)_{\text{new}}$.
3. Step 2 is repeated until convergence is reached, i.e. $\tau^*_{ij} \approx \left(\tau^*_{ij}\right)_{\text{new}}$ within a tolerance level, or until the maximum number of iterations is reached.

The smoothness parameter λ can be estimated through a stability analysis. In this procedure, the minimum and maximum delay values of the matrix are inspected for increasing λ (see Fig. 9, right). The appropriate value of λ is the point at which the minimum and maximum delay values no longer change for an increment of λ.

Appendix B. Local maximum based correlation analysis

The recordings of patient 7 in this study reflected a large variability in the shape of the IEDs, demonstrating multiple activated brain areas (see Fig. 8). Due to this high variability the regularization procedure in Appendix A did not lead to plausible results for delay estimation. To resolve this issue, a re-evaluation is performed of the correlation function $h^2_{ij}(w_k, \tau_{ij})$. The first step is the detection of the local maxima of the correlation function. In order to prevent the detection of maxima caused by with noise, only the local maxima that survived a blurring of scale $\sigma = 10$ (corresponding to a kernel of size 10 ms) were maintained. The results of local maxima detection for both $h^2_{ij}(w_k, \tau_{ij})$ and its transpose $h^2_{ji}(w_k, \tau_{ij})$ are shown in Fig. 10. Subsequently, the locations of the local maxima and their correlation coefficient are included in a weighted distribution, where each delay at the q-th local maximum $\tau_q = \tau_{ij}(w_k, q)$ is weighted by its corresponding correlation $h^2_q = h^2_{ij}(w_k, \tau_q)$. The delay between any two EEG signals i and j is then estimated by the weighted arithmetic mean according to $\hat{\tau}_{ij} = \frac{1}{k}\sum_k^{\#\text{IEDs}} \frac{1}{q}\left(\sum_q^{\#\text{maxima}} h^2_q \tau_q\right) \Big/ \left(\sum_q^{\#\text{maxima}} h^2_q\right)$.

Since the correlation function for an individual spike may contain noise, several preprocessing enhancement steps are applied. Firstly, a second-order Gaussian derivative filter with scale $\sigma = 10$ is applied to the monopolar EEG data for each spike. This procedure enhances the spike amplitude while reducing low-amplitude background activity. Furthermore, since low-frequency background activity is known to produce relatively high correlation in some cases, a total variation measure is applied to weigh the correlation function according to EEG activity. In practice this

leads to a reduction of peaks in the correlation function associated with background activity. The correlation function for each spike is weighted according to $h_{ij}^2(w_k, \tau_{ij}) \cdot \log(\mathrm{TV}_{w_k,i}/\mathrm{TV}_{w_k,ref})$, where TV is the total variation $\mathrm{TV}_{w_k,i} = \sum_{t=0}^{T} \|y_i'(t)\|$ and y_i is the EEG signal for the ith channel within window w_k and T is the time length of the window. The derivative y_i' is calculated by a first-order Gaussian derivative filter ($\sigma = 5$). The total variation for a given channel i is compared to a reference value $\mathrm{TV}_{w_k,ref}$ that is associated with background activity. The logarithm is used in order to get a weighting that is zero when the total variation is equal to the reference.

For the case of patient 7, we are particularly interested in the delays relative to the RY electrode. Since there may be variation in the used reference signal j, three reference electrodes RY9, RY10 and RY11 are used, which displayed similar activity throughout all spikes. The results corresponding to the second cluster of patient 7 (see Fig. 8) are shown in Fig. 11 for the delay of every electrode with respect to the reference electrode RY (A) and the transposed delay estimation (B). It can be observed that the two results are approximately anti-symmetric and behave according to the condition $\tau_{IJ} \approx -\tau_{JI}$, where I and J denote whole electrodes, which enforces the reliability of the delay computation. The end result is computed by the averaged norm of both delays according to $\tau_{I \leftrightarrow J} = \frac{1}{2}\left(\sum_i^{\#\text{electrodes}} \|\tau_{IJ}\| + \sum_i^{\#\text{electrodes}} \|\tau_{JI}\|\right)$, shown in Fig. 11C.

References

Alarcon G, Guy CN, Binnie CD, Walker SR, Elwes RD, Polkey CE. Intracerebral propagation of interictal activity in partial epilepsy: implications for source localisation. J Neurol Neurosurg Psychiat 1994;57(4):435–49.

Amini L, Jutten C, Achard S, David O, Soltanian-Zadeh H, Hossein-Zadeh GA, et al. Directed differential connectivity graph of interictal epileptiform discharges. IEEE Trans Biomed Eng 2011;58(4):884–93.

Bartolomei F, Wendling F, Bellanger JJ, Régis J, Chauvel P. Neural networks involving the medial temporal structures in temporal lobe epilepsy. Clin Neurophysiol 2001;112(9):1746–60.

Bartolomei F, Wendling F, Chauvel P. The concept of an epileptogenic network in human partial epilepsies. Neurochirurgie 2008;54(3):174–84.

Bartolomei F, Gavaret M, Hewett R, Valton L, Aubert S, Regis J, et al. Neural networks underlying parietal lobe seizures: a quantified study from intracerebral recordings. Epilepsy Res 2011;93(2–3):164–76.

Bartolomei F, Trebuchon A, Bonini F, Lambert I, Gavaret M, Woodman M, et al. What is the concordance between the seizure onset zone and the irritative zone? A SEEG quantified study. Clin Neurophysiol 2016;127(2):1157–62.

Bartolomei F, Lagarde S, Wendling F, McGonigal A, Jirsa V, Guye M, et al. Defining epileptogenic networks: contribution of SEEG and signal analysis. Epilepsia 2017;58(7):1131–47.

Bettus G, Wendling F, Guye M, Valton L, Régis J, Chauvel P, et al. Enhanced EEG functional connectivity in mesial temporal lobe epilepsy. Epilepsy Res 2008;81(1):58–68.

Bourien J, Bartolomei F, Bellanger JJ, Gavaret M, Chauvel P, Wendling F. A method to identify reproducible subsets of co-activated structures during interictal spikes. Application to intracerebral EEG in temporal lobe epilepsy. Clin Neurophysiol 2005;116(2):443–55.

Bullmore E, Sporns O. Complex brain networks: graph theoretical analysis of structural and functional systems. Nat Rev Neurosci 2009;10(3):186–98.

da Silva FL. Interdependence of EEG signals: linear vs nonlinear associations and the significance of time delays and phase shifts. Brain Topogr 1989;2(1/2):9–18.

da Silva Braga AM, Fujisao EK, Betting LE. Analysis of generalized interictal discharges using quantitative EEG. Epilepsy Res 2014;108(10):1740–7.

de Curtis M, Jefferys JGR, Avoli M. Interictal epileptiform discharges in partial epilepsy: complex neurobiological mechanisms based on experimental and clinical evidence. In: Jasper's basic mechanisms of the epilepsies; 2012.

Delorme A, Makeig S. EEGLAB: an open source toolbox for analysis of single-trial EEG dynamics including independent component analysis. J Neurosci Methods 2004;134(1):9–21.

Dyrholm M, Makeig S, Hansen LK. Model selection for convolutive ICA with an application to spatiotemporal analysis of EEG. Neural Comput 2007;19(4):934–55.

Højen-Sørensen PADFR, Winther O, Hansen LK. Mean-field approaches to independent component analysis. Neural Comput 2002;14(4):889–918.

Hyvarinen A, Oja E. Independent component analysis: algorithms and applications. Neural Netw 2000;13(4–5):411–30.

Jutten C, Herault J. Blind separation of sources. Part I: An adaptive algorithm based on neuromimetic architecture. Sign Process 1991;24(1):1–10.

Kahane P, Bartolomei F. Temporal lobe epilepsy and hippocampal sclerosis: lessons from depth EEG recordings. Epilepsia 2010;51(Suppl 1):59–62.

Kalitzin SN, Parra J, Velis DN, Lopes da Silva FH. Quantification of unidirectional nonlinear associations between multidimensional signals. IEEE Trans Biomed Eng 2007;54(3):454–61.

Lindeberg T. Scale-space theory in computer vision. Dordrecht (The Netherlands): The Kluwer International Series in Engineering and Computer Science; 1994.

Lipping T, Ferenets R, Puumala P, Suominen K, Karvonen E, Sonkajarvi E, et al. EEG independent component and coherence analysis from scalp and depth electrodes during propofol anesthesia. In: Conf proc IEEE eng med biol soc, vol. 3; 2003, pp. 2471–2474.

Makeig S, Jung T-P, Bell AJ, Ghahremani D, Sejnowski TJ. Blind separation of auditory event-related brain responses into independent components. Proc Natl Acad Sci 1997;94(20):10979–84.

Marinazzo D, Liao W, Chen H, Stramaglia S. Nonlinear connectivity by granger causality. Neuroimage 2011;58(2):330–8.

Meesters S, Ossenblok P, Wagner L, van Houdt P, Colon A, Schijns O, et al. Visualization of synchronized stereoencephalographic recordings in a 3D smart image to aid presurgical evaluation of epilepsy. Front Neuroinform 2014.

Mohanraj R, Brodie MJ. Diagnosing refractory epilepsy: response to sequential treatment schedules. Eur J Neurol 2006;13(3):277–82.

Oostenveld R, Fries P, Maris E, Schoffelen J-M. Fieldtrip: open source software for advanced analysis of MEG, EEG, and invasive electrophysiological data. Comput Intell Neurosci 2011;2011:9.

Otsu N. A threshold selection method from gray-level histograms. IEEE Trans Syst Man Cybern 1979;9(1):62–6.

Pereda E, Quiroga RQ, Bhattacharya J. Nonlinear multivariate analysis of neurophysiological signals. Prog Neurobiol 2005;77(1–2):1–37.

Pijn J, Lopes da Silva F. Propagation of electrical activity: nonlinear associations and time delays between EEG signals. Boston: Birkhäuser; 1993. p. 41–61.

Qin A, Suganthan P. Robust growing neural gas algorithm with application in cluster analysis. Neural Netw 2004;17(8):1135–48 [New Developments in Self-Organizing Systems].

Sanei S, Chambers JA. EEG signal processing. Wiley; 2007.

Smith SJM. EEG in the diagnosis, classification, and management of patients with epilepsy. J Neurol Neurosurg Psychiatr 2005;76(suppl 2):ii2–7.

Stam C, van Straaten E. The organization of physiological brain networks. Clin Neurophysiol 2012;123(6):1067–87.

Talairach J, Tournoux P, Musolino A, Missir O. Stereotaxic exploration in frontal epilepsy. Adv Neurol 1992;57:651–88.

Tibshirani R, Walther G, Hastie T. Estimating the number of clusters in a data set via the gap statistic. J Roy Stat Soc Ser B Stat Methodol 2001;63(2):411–23.

van Houdt PJ, Ossenblok PPW, Colon AJ, Boon PAJM, de Munck JC. A framework to integrate EEG-correlated fMRI and intracerebral recordings. Neuroimage 2012;60(4):2042–53.

van Houdt PJ, de Munck JC, Leijten FS, Huiskamp GJ, Colon AJ, Boon PA, et al. EEG-fMRI correlation patterns in the presurgical evaluation of focal epilepsy: a comparison with electrocorticographic data and surgical outcome measures. Neuroimage 2013;75(238–248).

Van 't Ent D, Manshanden I, Ossenblok P, Velis DN, de Munck JC, Verbunt JPA, et al. Spike cluster analysis in neocortical localization related epilepsy yields clinically significant equivalent source localization results in magnetoencephalogram (MEG). Clin Neurophysiol 2003;114(10):1948–62.

Ward JH. Hierarchical grouping to optimize an objective function. J Am Stat Assoc 1963;58(301):236–44.

Wendling F, Bartolomei F. Modeling EEG signals and interpreting measures of relationship during temporal-lobe seizures: an approach to the study of epileptogenic networks. Epileptic Disord 2001;Special Issue:67–78.

Wendling F, Bartolomei F, Bellanger JJ, Chauvel P. Interpretation of interdependencies in epileptic signals using a macroscopic physiological model of the EEG. Clin Neurophysiol 2001a;112(7):1201–18.

Wendling F, Bartolomei F, Bellanger JJ, Chauvel P. Identification of epileptogenic networks from modeling and nonlinear analysis of SEEG signals. Neurophysiol Clin 2001b;31(3):139–51.

Wendling F, Bartolomei F, Senhadji L. Spatial analysis of intracerebral electroencephalographic signals in the time and frequency domain: identification of epileptogenic networks in partial epilepsy. Philos Trans Phys Sci Eng 2009;367(1887):297–316.

Wendling F, Chauvel P, Biraben A, Bartolomei F. From intracerebral EEG signals to brain connectivity: identification of epileptogenic networks in partial epilepsy. Front Syst Neurosci 2010;4:154.

Yekutieli D, Benjamini Y. Resampling-based false discovery rate controlling multiple test procedures for correlated test statistics. J Stat Plan Inference 1999;82(1–2):171–96.